LETTER
PLANETARY SCIENCES

Earth and Planetary Physics
6: 284–293, 2022
doi: 10.26464/epp2022026

A two-dimensional energy balance climate model on Mars

YaoKun Li[1]*, and JiPing Chao[2]

[1]College of Global Change and Earth System Science, Beijing Normal University, Beijing 100875, China;

[2]National Marine Environmental Forecasting Center, Beijing 100081, China

Key Points:

- We build a two-dimensional energy balance model to investigate the climate on Mars.
- The model can simulate reasonable surface atmospheric temperature distribution.
- The model can be applied in discussing effects of the solar radiation, dust and surface albedo.

Citation: Li, Y. K., and Chao, J. P. (2022). A two-dimensional energy balance climate model on Mars. *Earth Planet. Phys.*, *6*(3), 284–293. http://doi.org/10.26464/epp2022026

Abstract: A two-dimensional energy balance climate model has been built to investigate the climate on Mars. The model takes into account the balance among solar radiation, longwave radiation, and energy transmission and can be solved analytically by Legendre polynomials. With the parameters for thermal diffusion and radiation processes being properly specified, the model can simulate a reasonable surface atmospheric temperature distribution but not a very perfect vertical atmospheric temperature distribution compared with numerical results, such as those from the Mars Climate Database. With varying solar radiation in a Martian year, the model can simulate the seasonal variation of the air temperature on Mars. With increasing dust content, the Martian atmosphere gradually warms. However, the warming is insignificant in the cold and warm scenarios, in which the dust mixing ratio varies moderately, whereas the warming is significant in the storm scenario, in which the dust mixing ratio increases dramatically. With an increasing albedo value of either the polar cap or the non-ice region, Mars gradually cools. The mean surface atmospheric temperature decreases moderately with an increasing polar ice albedo, whereas it increases dramatically with an increasing non-ice albedo. This increase occurs because the planetary albedo of the ice regions is smaller than that of the non-ice region.

Keywords: Mars; energy balance climate model; solar radiation; dust; surface albedo

1. Introduction

Humanity has long been fascinated by the planet Mars (Haberle et al., 2017). The present name comes from the Roman god of war in western culture. Mars was called "Yinghuo" in ancient China to describe its glowing light and uncertain whereabouts. Our knowledge of Mars has accumulated dramatically in the past 40 years because of the wealth of information provided by Mars orbiters, landers, and rovers (Barlow, 2014), and it will continue to increase. The three most recently launched spacecrafts are exploring the planet by the time this article is published. These include humans' first successful unmanned flight by the Ingenuity helicopter released from NASA's Perseverance Mars rover; China's first Martian probe, Tianwen-1, released by China's first Mars rover, Zhurong, which has successfully completed its established mission and continues to explore the planet (e.g., Liu K et al., 2020; Peng YQ et al., 2020); and the Al-Amal probe, the first Mars probe launched by the United Arab Emirates.

Mars has always played a prominent role in such comparative studies with the Earth because the two planets share the fundamental properties of rapid rotation, similar atmospheres that are largely heated by a radiative and convective exchange with the surface, and a seasonal progression of the climate (Haberle et al., 2017). The fact that the Martian atmosphere is mostly driven by radiation has long been the mainstream understanding. However, this assumption has recently been challenged by a large eddy simulation study by Wu ZP et al. (2021), who pointed out that positive feedback exists between the dust optical depth and the vigor and depth of convective boundary layer mixing. Leovy and Mintz (1969) adapted a two-level model for planetary atmospheres to build the first-generation Mars general circulation model (MGCM). The model was developed and applied to address issues of heat balance in the Martian polar region (Pollack et al., 1990) and the atmospheric dynamics, such as the zonal mean circulation (Haberle et al., 1993), transient baroclinic eddies and winter quasi-stationary eddies (Barnes et al., 1996), and dust storms (Murphy et al., 1995; Hollingsworth et al., 1996). In addition, two groups from the Laboratoire de Météorologie Dynamique (LMD, Paris) and the Sub-department of Atmospheric, Oceanic and Planetary Physics at Oxford University (AOPP, Oxford) had collaborated to develop a new-generation MGCM, based largely on the models previously developed separately by the two groups (Forget et al., 1999). They constructed a Mars Climate Database (MCD; Read et al., 1997; Lewis et al., 1999) that can be applied in investigations such as the effect of dust storms, simula-

Correspondence to: Y. K. Li, liyaokun@bnu.edu.cn
Received 17 JAN 2022; Accepted 28 MAR 2022.
Accepted article online 08 APR 2022.

tions of geometric albedo spectra (Smith et al., 2020), and gravity wave activity in the lower atmosphere of Mars (Heavens et al., 2020). To address some of the limitations of the MCD, the Open access to Mars Assimilated Remote Soundings (OpenMARS) data set was recently created for use as a reference data set of actual global weather that occurred on Mars from 1999 to 2015 (Holmes et al., 2020). The MGCM has greatly promoted the investigation of the red planet and our understanding of it.

Nevertheless, it is still necessary to apply some simple models to highlight the thermodynamics and dynamics of specific physical processes. Considering that the energy balance between incoming solar radiation and outgoing longwave radiation determines the temperature on Mars, a major part of what is meant by climate (Pierrehumbert, 2010), the energy balance model (EBM) is a good candidate. For example, Hoffert et al. (1981) investigated liquid water on Mars by developing a theoretical EBM that includes the meridional heat flux proposed by Budyko (1969), Sellers (1969), and North (1975). Nakamura and Tajika (2001, 2002) studied the stability and evolution of the climate system of Mars under annual and seasonal solar radiation incomes. Savijärvi (2014) constructed a "toy climate model" (in fact, an EBM) for Mars from a surface energy budget to simulate midday surface and near-surface air temperatures. Taubenberger (2020) calculated the surface temperature on Mars by applying the classic Budyko–Sellers-type EBM with a realistic albedo. Generally speaking, EBMs are applicable for the zonal mean surface temperature. They can be extended to be two-dimensional by adding either the longitudinal or vertical distribution. For the vertical distribution, a common practice is to introduce the classic radiative–convective equilibrium, the analytic solution of which is difficult to derive. Another useful practice is to solve the simplified temperature equation analytically. For example, Lü YH and Chao JP (1981) built a two-dimensional EBM by applying a simplified scheme for the radiative transfer equation proposed by Kuo HL (1973). However, they provided only a few calculation examples and left the two-dimensional temperature distribution undiscussed. They also did not consider some important physical factors, such as dust and water-ice clouds.

Considering that the knowledge of Mars has advanced greatly during the past decades, this work attempts to update the two-dimensional EBM of Lü YH and Chao JP (1981) by adding more specific physical processes. The remainder of this paper is organized as follows. The two-dimensional EBM framework is introduced in Section 2, along with the effects of dust and CO_2 on the absorption of solar and longwave radiation. The theoretical temperature distributions for different Martian seasons are then calculated and discussed in Section 3. Finally, conclusions and a discussion are presented in Section 4.

2. The Two-Dimensional EBM

2.1 Temperature Equation

By considering the balance between the turbulent heat flux and the radiation flux, the temperature equation (e.g., Lü YH and Chao JP, 1981; Li YK and Chao JP, 2014) can be written as

$$\frac{\kappa_h}{a^2}\frac{\partial}{\partial x}\left(1-x^2\right)\frac{\partial T}{\partial x}+\frac{\partial}{\partial z}\left(\kappa_z\frac{\partial T}{\partial z}\right)+\sum_j k_j\left(A_j+B_j-2E_j\right)+k'Q=0, \quad (1)$$

where κ_h, κ_z are the horizontal and vertical turbulent thermal conductivity; k_j is the longwave radiation absorption coefficient at wavelength λ_j; A_j, B_j, and E_j are the corresponding downward and upward longwave radiation and the black body radiation at wavelength λ_j; k' is the mean bulk absorption coefficient of the solar radiation; Q is the downward solar radiation; $x=\sin\phi$, where ϕ is latitude; and a is the radius of Mars. Equation (1) involves the summation of the entire radiation absorption spectrum, which is too complex to derive an analytic solution. To simplify the derivation and to highlight the physical meanings of the radiation processes, Kuo HL (1973) proposed a method to divide the entire radiation absorption spectrum into strong and weak zones (denoted by the subscripts s and w, respectively). He assumed $k_w^2 \ll \partial^2/\partial z^2 \ll k_s^2$ so that k_w^2 can be neglected with respect to $\partial^2/\partial z^2$, whereas $\partial^2/\partial z^2$ can be neglected in comparison with k_s^2. By applying this simplification scheme, Equation (1) can be transformed to

$$D\frac{\partial}{\partial x}\left(1-x^2\right)\frac{\partial E}{\partial x}+\left(\kappa_z+\kappa_r\right)\frac{\partial^2 E}{\partial \xi^2}-N^2E=-\tilde{S}\bar{Q}_0\xi_0 e^{-\xi_0\xi}S(x)+\tilde{S}\bar{Q}_0C, \quad (2)$$

where $D=\frac{\xi_0^2\kappa_h}{k'^2a^2}$, $\tilde{S}=\frac{4\xi_0\sigma\bar{T}^3}{k'}$, $\kappa_r=\frac{8r\sigma\bar{T}^3}{k_s}$, $N^2=\frac{8(1-r)k_w\xi_0^2\sigma\bar{T}^3}{k'^2}$, $\xi=\frac{1}{\xi_0}\int_z^\infty k'\mathrm{d}z$, $\xi_0=\int_0^\infty k'\mathrm{d}z$, $C=r\left(1+\frac{k'}{k_w}\right)\bar{\Pi}_0+\left(\bar{\Pi}_1-\bar{\Pi}_0+1-e^{-\xi_0}\right)$, $\bar{\Pi}_0=\int_0^1\Pi_0S(x)\mathrm{d}x$, $\bar{\Pi}_1=\int_0^1\Pi_1S(x)\mathrm{d}x$, $\Pi_0=1-\Gamma_p$, and $\Pi_1=1-\Gamma_p-\left(1-e^{-\xi_0}\right)$. In addition, $E_{s,w}=\int_{s,w}E_\lambda\mathrm{d}\lambda$ is the mean black body radiation in strong and weak absorption regions, $k_{s,w}=\int_{s,w}k_\lambda E_\lambda\mathrm{d}\lambda/E_{s,w}$ are the mean absorption coefficients in strong and weak absorption regions, and $r=E_s/E$ is the proportion of the strong absorption zone to the entire absorption spectrum. $\bar{Q}_0$ is the mean solar radiation at the top of atmosphere (TOA) of Mars and $S(x)$ is its zonal mean nondimensional distribution. Variable ξ is the optical depth, and ξ_0 is the global mean optical depth at the surface. It shows the absorption capacity of the Martian atmosphere to solar radiation. Variable Γ_p is the planetary albedo. Therefore, Π_0 and Π_1 represent the proportion of net solar radiation arriving at the TOA and at the surface, respectively. $\bar{\Pi}_0$ and $\bar{\Pi}_1$ are their global mean values. One can refer to Li YK and Chao JP (2014) for more detailed information. By specifying the upper and lower boundary conditions,

$$\int_0^1 E_0\mathrm{d}x=\frac{1}{2}\left(1+\frac{k'}{k_w}\right)\bar{\Pi}_0\bar{Q}_0, \quad (3)$$

$$\left(\kappa_z+\kappa_r\right)\frac{\partial E}{\partial \xi}=N^2\int_0^1 E\mathrm{d}\xi-2(1-r)\tilde{S}E_0+\tilde{S}\bar{Q}_0\left(\frac{k'}{k_w}\Pi_0+\Pi_1\right)S(x), \quad (4)$$

Equation (2) can be solved analytically by expanding the solution to the Legendre series.

2.2 Solar Radiation Distribution

The instantaneous beam irradiance at the Mars TOA (Appelbaum et al., 1993) is

$$S=\bar{S}_0\frac{\left[1+e\cos\left(L_s-248^\circ\right)\right]^2}{\left(1-e^2\right)^2}\left(\sin\phi\sin\delta+\cos\phi\cos\delta\cos\omega\right), \quad (5)$$

where $\bar{S}_0$ is the Mars solar constant ($\bar{S}_0=590\ \mathrm{W/m^2}$), e is the ec-

centricity of Mars (e = 0.009377), and L_s is the areocentric longitude. When Mars arrives at its perihelion, L_s equals 248°. Variable δ is the declination angle, and ω is the hour angle measured from true noon westward. The solar declination angle is given by $\sin\delta = \sin\delta_0 \sin L_s$, where δ_0 is the obliquity of the Mars rotational axis (δ_0 = 24.936°). By integrating Equation (5) from sunrise to sunset of a Martian day, we can derive the daily total solar irradiation (TSI) at the Mars TOA at any latitude. Further, by integrating the daily TSI for a complete orbit cycle, we can derive the annual mean TSI at the Mars TOA (Figure 1a). We can find that the annual mean TSI, or mean solar radiation at the Mars TOA, is not symmetric around the equator because of its large eccentricity. The maximum value is located near the equator in the southern hemisphere. This is a major difference compared with the Earth, where the annual mean TSI is basically symmetric around the equator. This asymmetric feature denotes the need to include the odd terms when expanding the TSI to the Legendre series,

$$Q_0 = \bar{Q}_0 \sum_{n=0}^{N} S_n P_n(x) \equiv \bar{Q}_0 S(x), \tag{6}$$

where S_n are the expansion coefficients, $P_n(x)$ are the Legendre polynomials, and N is the expansion order. We find that N = 4 is good sufficient to fit the annual mean distribution. In addition, we set the mean solar radiation in months 1, 4, 7, and 10 to present different seasons on Mars. Here, a month is defined as the 30° areocentric longitude range, and month 1 begins from 0°. Under this definition, a Martian year will have 12 months, similar to a year on the Earth.

2.3 Dust Distribution

Now let us deal with the transmission of the solar radiation. Dust is the main absorption medium for solar radiation, in contrast to water vapor on Earth. A classic suspended dust distribution is given by Conrath (1975):

$$q = q_0 \exp\{v[1 - \exp(z/H)]\}, \tag{7}$$

where q_0 is the dust mixing ratio at the surface, v is a parameter modifying the vertical profile and is often taken to be 0.007, and H is the scale height of the Martian atmosphere and is often assumed to be 10 km. To better represent a realistic vertical distribution, Forget et al. (1999) modified Equation (7) to

$$q = q_0 \exp\left[v(1 - p_0/p)^{(70/z_{\max})}\right], \tag{8}$$

where $z_{\max}$ is the altitude (km) of the top of the dust layer; $p_0/p = \exp(z/H)$ is the log pressure, and p_0 is a reference pressure level (e.g., 700 Pa). If $z_{\max}$ = 70 km, Equation (8) reduces to the Conrath form of Equation (7). Variable $z_{\max}$ can be a function of the areocentric longitude L_s and latitude ϕ; for example, Forget et al. (1999) summarized a function $z_{\max} = 60 + 18\sin(L_s - 160°) - 22\sin^2\phi$. However, we still apply Equation (7) in the model rather than this complex form.

Once the dust distribution is specified, the dust optical depth can be calculated:

$$\xi_0 = \int_0^\infty k' \mathrm{d}z = \int_0^\infty k'_d \rho_a q \mathrm{d}z, \tag{9}$$

where k'_d is the mean mass absorption coefficient of dust for solar radiation and ρ_a is the density of the atmosphere. In calculating the whole-layer optical depth of the dust, q_0 is generally taken as a constant (e.g., 5×10^{-4}, as Heavens et al., 2011, and Wang C et al., 2018, suggested), although it varies spatially. The Martian atmosphere absorbs approximately 9% of the incoming solar

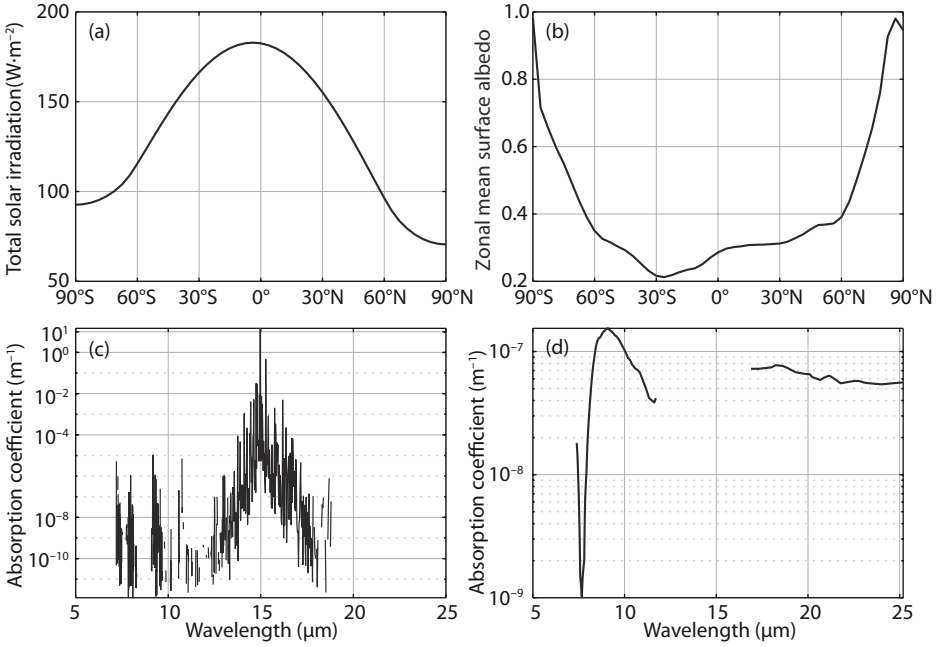

Figure 1. Zonal mean solar radiation (a), zonal mean surface albedo from the Mars Climate Database (b), CO_2 absorption spectra (c) from the high-resolution transmission molecular absorption database (HITRAN) website (https://hitran.iao.ru/), and dust absorption spectra from Smith (2004) (d). Notice that the spectral values near 15 μm are not portrayed because of the extremely strong absorption by CO_2 in the 15 μm band.

radiation, which includes approximately 8% absorbed by dust and 1% absorbed by clouds and other gases (Haberle et al., 2017). This indicates that the absorption optical depth for solar radiation is approximately 0.09, namely, $\xi_0 = 0.09$, which is basically consistent with the results by Montabone et al. (2015) derived from observation and with the results ($\xi_0 = 0.1$) provided by Millour et al. (2008) in their Detailed Design Document for version 4.3 of the MCD. On the basis of the references above, the value of the absorption optical depth for solar radiation is set to 0.1. The value of the surface atmospheric density is set to 0.0174 kg·m^{-3} according to the MCD. We can then derive the mean dust mass absorption coefficient for solar radiation $k_d' = 61.6$ m^2·kg^{-1}, which is basically consistent with the values derived by Heavens et al. (2011) in order. In a later calculation, k_d' is set as a constant, whereas q_0 can vary to represent different dust concentrations in the atmosphere.

2.4 Surface Albedo Distribution

Similar to Earth, Mars has ice caps in polar regions. Unlike the Earth, the caps are mainly composed of CO_2 ice. The albedo values vary greatly in the polar ice regions and the ice-free regions (Figure 1b). Therefore, referring to the common practice of EBMs, the surface albedo distribution function is given as

$$\alpha_s = \begin{cases} \alpha_i, & x_n < x < 1 \\ \alpha_f, & x_s < x < x_n \\ \alpha_i, & -1 < x < x_s \end{cases}, \tag{10}$$

where α_i is the albedo of the polar ice cap, α_f is the albedo of the non-ice region, $x_s = \sin\phi_s$, $x_n = \sin\phi_n$, and ϕ_s and ϕ_n are ice lines in the southern and northern hemisphere, respectively. The polar ice albedo value varies from 0.45 to 0.75 in different literature studies (e.g., Pollack et al., 1981; James and North, 1982; Haberle et al., 1994; Clifford et al., 2000; Nakamura and Tajika, 2001). The reference CO_2 ice cap albedo in this article is chosen as 0.6. The ice-free land albedo is set to 0.18, a little lower than the 0.25 set by Haberle et al. (1994) and the 0.215 set by Pollack et al. (1987). They chose a relatively larger value in their one-dimensional EBM to represent the Mars planetary albedo, which is set as a constant; for example, a commonly used value is $\Gamma_p = 0.25$ (Barlow, 2014; Haberle et al., 2017). In the two-dimensional EBM adopted in this research, we not only considered the surface albedo, but also the clouds and dust albedo. Equation (10) suggests asymmetric ice line latitudes around the equator in each hemisphere. If setting $x_s = -x_n$, it reduces to the symmetric situation as applied by Nakamura and Tajika (2001, 2002). By estimating from the results of Titus and Cushing (2014), Piqueux et al. (2015), and Haberle et al. (2017), we chose $\phi_n = 70$°N and $\phi_s = 60$°S. These values are comparable to those of Nakamura and Tajika (2001, 2002), who used a symmetric 70° to denote the ice line. On the basis of the values above, the mean surface albedo value is approximately 0.21, which is basically consistent with that of Haberle et al. (2017). By subtracting the mean surface planetary albedo from the planetary albedo, we can then determine that the clouds and dust albedo value is approximately 0.04, basically the same as that of Haberle et al. (2017) but smaller than the value (0.124) used by Pollack et al. (1981). We also tested the sensitivity of the surface albedo by changing the albedo values of the polar ice and ice-free region.

2.5 Longwave Radiation Scheme

Unlike with solar radiation, CO_2 and dust are the main absorbers of longwave radiation. The total absorption coefficient can be written as

$$k = k_{CO_2}\rho_a + k_{dust}\rho_a q, \tag{11}$$

where k_{CO_2} and k_{dust} are the mass absorption coefficients for CO_2 and dust. It should be noted that water-ice clouds are also an important absorber of longwave radiation. Considering that the amount of water-ice clouding on Mars is relatively small, we do not take its effect into consideration right now. The spectrum k_{CO_2} (Figure 1c) can be obtained from the high-resolution transmission molecular absorption database (HITRAN) website (https://hitran.iao.ru/). The dust spectrum (Figure 1d) comes from the results of Smith (2004), who gave a nondimensional amplitude with respect to the wavenumber of 1,075 cm^{-1}. He further suggested a reference value of approximately 0.15 for the dust optical depth at 1,075 cm^{-1}. According to the definition of optical depth in Equation (9), we can easily determine that the dust mass absorption coefficient at 1,075 cm^{-1} is 1.78 m^2·kg^{-1}. The dust absorption spectrum can then be totally known. By dividing the total absorption spectrum by 4×10^{-6} m^{-1}, we can determine that k_s = 41.6 m^{-1}, $k_w = 1.79\times10^{-5}$ m^{-1}, and $r = 0.071$. This result suggests that although strong absorptive regions have a relatively large absorption coefficient, they account for only a very small part of the entire absorption spectrum. This can also be seen directly in Figures 1b–1c. By specifying the proper horizontal and vertical turbulent thermal conductivity (e.g., $\kappa_h = 6\times10^5$ W·m^{-1}·K^{-1}, $\kappa_z = 4\times10^4$ W·m^{-1}·K^{-1}), we can obtain a reasonable temperature distribution.

3. Results

As discussed above, we conducted two control experiments in which all the variables were set to the climatological mean (Exp1) and monthly mean climatological values (Exp2) to represent the climatological atmospheric temperature distribution. We then conducted three additional experiments (Exp3–Exp5) to further calculate the atmospheric temperature distribution in cold, warm, and storm scenarios that differed in dust content to test the reliability of the model. We designed the last two experiments (Exp6–Exp7) to test the sensitivity of the introduced surface albedo values. At present, the surface albedo of Mars does not have significant variations. However, the surface of Mars has undergone dramatic changes on a very long term time scale. Therefore, these two experiments may provide useful information for understanding the climate evolution on a very long term time scale. A detailed description of the experimental design is summarized in Table 1.

As shown in Figure 2a, the mean surface atmospheric temperature is approximately 210 K at the equator and declines to approximately 150 K at the south pole and to approximately 160 K at the north pole (solid line in Figure 2a). These temperatures fit well with the mean surface atmospheric temperature in the MCD (dashed line in Figure 2a) and suggest that the model has the reliability to simulate a reasonable surface atmospheric temperature. However, some deficiencies exist in the vertical distribution. We can see that the theoretical atmospheric temperature generally

Table 1. Description of the experiments conducted.

Exp. no.	Solar radiation	Dust content	Surface albedo
Exp1	Climatological	q_0	α_i, α_f
Exp2	Monthly	Monthly	α_i, α_f
Exp3	Climatological	Cold scenario	α_i, α_f
Exp4	Climatological	Warm scenario	α_i, α_f
Exp5	Climatological	Storm scenario	α_i, α_f
Exp6	Climatological	q_0	α_i varies, α_f
Exp7	Climatological	q_0	α_i, α_f varies

Note. Variable q_0 represents the climatological dust mixing ratio. Variables α_i, α_f are the albedo values of polar ice and non-ice, respectively.

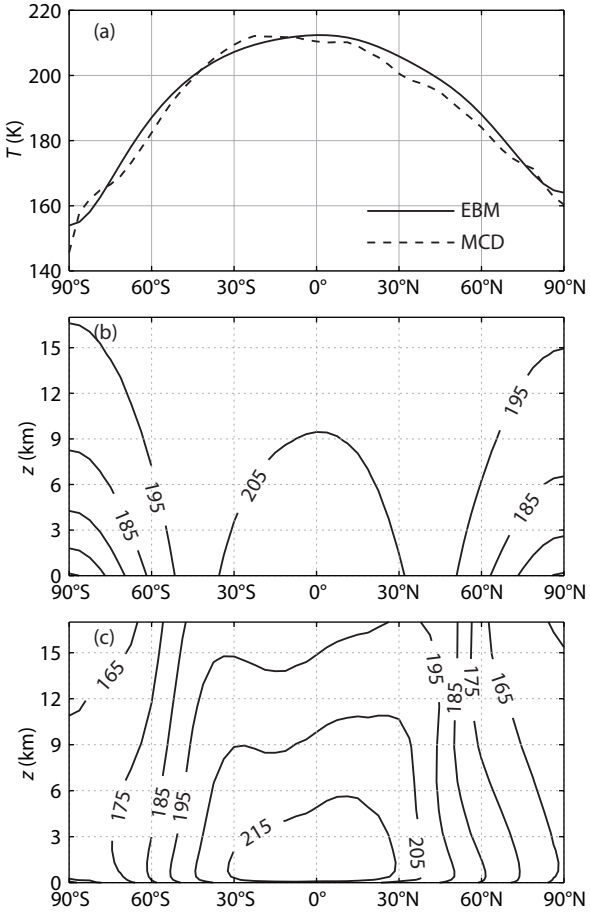

Figure 2. Climatological mean surface atmospheric temperature (a), climatological mean atmospheric temperature distribution of the two-dimensional energy balance model (EBM) (b) and of the Mars Climate Database (MCD) (c). The solid and dashed lines in (a) denote the surface atmospheric temperature for the two-dimensional EBM and the MCD, respectively.

declines monotonically with altitude, with a smaller lapse rate at low latitudes and a larger one at middle and high latitudes (Figure 2b). Significant differences exist comparing with the MCD, in which a strong temperature inversion occurs near the ground and the temperature lapse rate is larger at low latitudes but smaller at middle and high latitudes (Figure 2c). Generally speaking, the theoretical model can represent the basic temperature distribution in the MCD, but with caveats in the vertical distribution.

By specifying the monthly solar radiation and dust content, we further calculated the monthly atmospheric temperature. In Figure 2, months 1, 4, 7 and 10 are selected to show the seasonal variation. In month 1, the solar radiation is basically symmetrical around the equator, determining a symmetrical temperature (Figure 3a). Compared with the corresponding month in the MCD (Figure 3e), the theoretical model captures the symmetrical feature but with a smaller lapse rate in the tropical regions and a larger one in the polar regions. In month 4, the warmest temperature moves to approximately 50°–60°N in the northern hemisphere (Figure 3b). Compared with the corresponding month in the MCD (Figure 3f), the vertical structure is imperfect and needs further improvement. In month 7, the solar radiation is again basically symmetrical around the equator but with a relatively large irradiation value. The warmest atmospheric temperature (Figure 3c) can exceed approximately 220 K near the equator. Because the theoretical model does not simulate the low temperature in the southern polar region, the meridional temperature distribution is smaller than in the MCD (Figure 3g). In month 10, the warmest temperature is located at approximately 40°S in the southern hemisphere (Figure 3d). This theoretical calculation captures the essential characteristics, but it lacks additional detail on the meridional and vertical temperature gradients because it does not consider the atmospheric dynamic processes compared with the MCD (Figure 3h). Therefore, the model may be more suitably applied in calculating the climatological mean atmospheric temperature distribution, especially the surface atmospheric temperature distribution. On the basis of such a consideration, we further calculated the mean surface air temperature in each month (Figure 4). We found that the model could predict the seasonable variation quite well. The mean surface air temperature declines to a minimum value in month 2 of approximately 183 K and climbs to the maximum value of approximately 200 K in month 9. The largest differences with the MCD appear in months 7 and 8.

Dust is one of the major absorbers of solar and longwave radiation. It plays a critical role in modulating the climate of Mars. The MCD includes three scenarios, which represent the cold, warm, and storm cases on Mars, respectively. Following the scenarios in the MCD, we conducted three experiments (Exp3–Exp5) by applying the dust mixing ratio in the corresponding MCD scenarios. In the cold scenario, the atmospheric temperature distribution (Figure 5a) basically shows little change compared with the climatological state (Figure 2b). The atmospheric temperature in the cold scenario in the MCD (Figure 5d) also changes little compared with its normal climatological state (Figure 2c). In the warm scenario, the situation is quite similar. The changes in atmospheric temperature (Figure 5b) are insignificant. The surface atmospheric temperature in the warm scenario in the MCD changes slightly, whereas the atmospheric temperature aloft varies greatly (Figure 5e). Because the vertical distribution of dust in the theoretical model is fixed, the theoretical calculation does not predict the vertical temperature distribution well. In the storm scenario, the atmospheric temperature warms significantly (Figure 5c). However, as in the warm scenario, the vertical temperature distri-

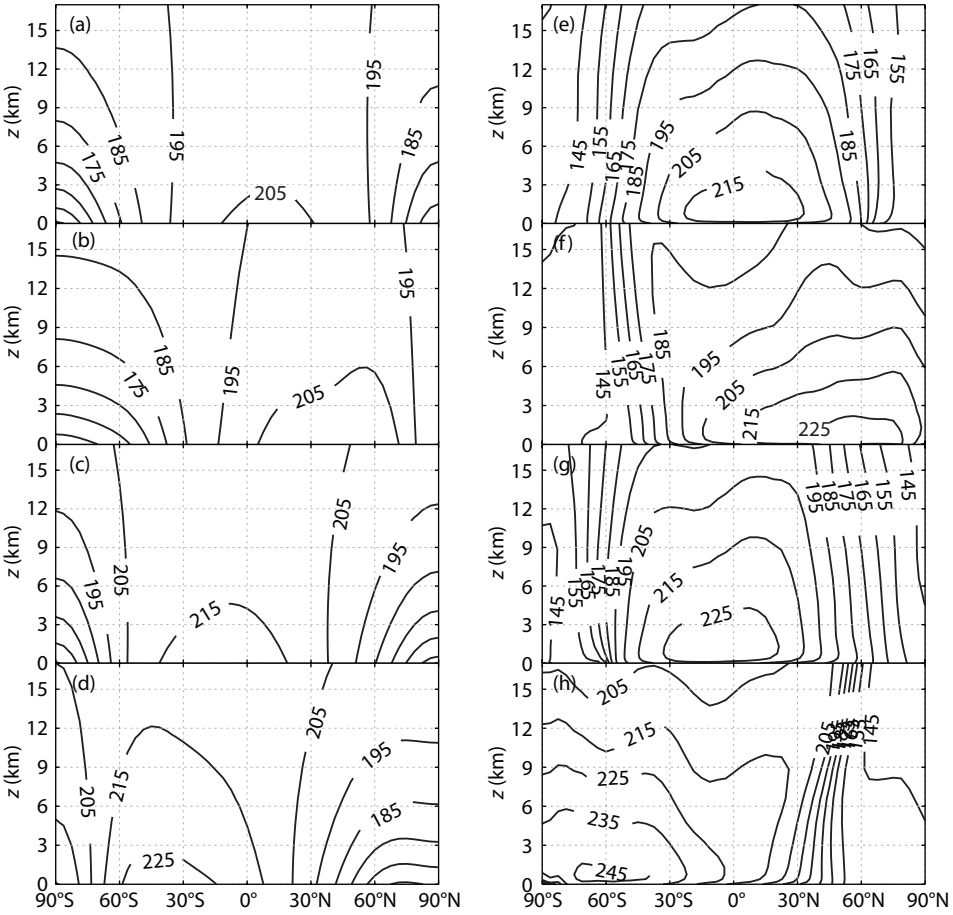

Figure 3. Atmospheric temperature distribution in month 1 (a, e), month 4 (b, f), month 7 (c, g), and month 10 (d, h). Panels (a–d) illustrate the results for the two-dimensional EBM, whereas panels (e–h) for the MCD.

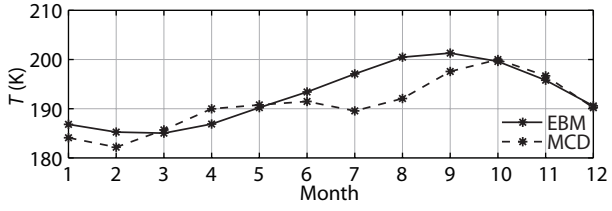

Figure 4. Variation of the mean surface atmospheric temperature with the month. The solid and dashed lines denote the two-dimensional EBM and the MCD, respectively.

bution violates the corresponding storm scenario in the MCD greatly (Figure 5f). Generally speaking, the theoretical calculation represents the surface atmospheric temperature well in all scenarios. However, it fails in predicting the vertical temperature distribution. This result may be caused by the specified vertical distribution of dust in the theoretical model and the lack of an atmospheric dynamic process.

We conducted another two experiments (Exp6 and Exp7) to test the climatic sensitivity to the surface albedo. In Exp6, we changed the albedo value of the polar CO_2 ice cap from 0.45 to 0.75, covering its general range of variation, as discussed previously. A small polar CO_2 ice albedo value (0.45) corresponds to a warm atmospheric temperature (Figure 6a). When the polar ice albedo value increases to 0.75, the atmospheric temperature declines in both the meridional and vertical directions (Figure 6b). The mean surface atmospheric temperature (Figure 6c) decreases from approximately 197 K to approximately 193 K. In Exp7, we changed the albedo value of the non-ice region from 0.1 to 0.3. A small albedo value (0.1) is associated with a warm atmosphere (Figure 7a), and the mean surface atmospheric temperature is approximately 200 K. When the albedo value is increased to 0.3, the atmosphere cools significantly (Figure 7b), and the mean surface air temperature is approximately 187 K. The mean surface air temperature basically decreases linearly (Figure 7c) with an increasing albedo value. Both cases suggest that the atmospheric temperature declines as the surface albedo increases because an increasing albedo at the surface will eventually increase the planetary albedo, which leads to more solar radiation being reflected into space. Furthermore, although the polar CO_2 ice albedo value is higher, the coverage of the polar ice cap is relatively smaller. Therefore, the contribution of polar ice to the planetary albedo is relatively small. The mean surface atmospheric temperature can be seen to decline by approximately 4 K when the polar ice cap albedo value increases from 0.45 to 0.75, whereas it declines by approximately 13 K when the albedo value of the non-ice region increases from 0.1 to 0.3.

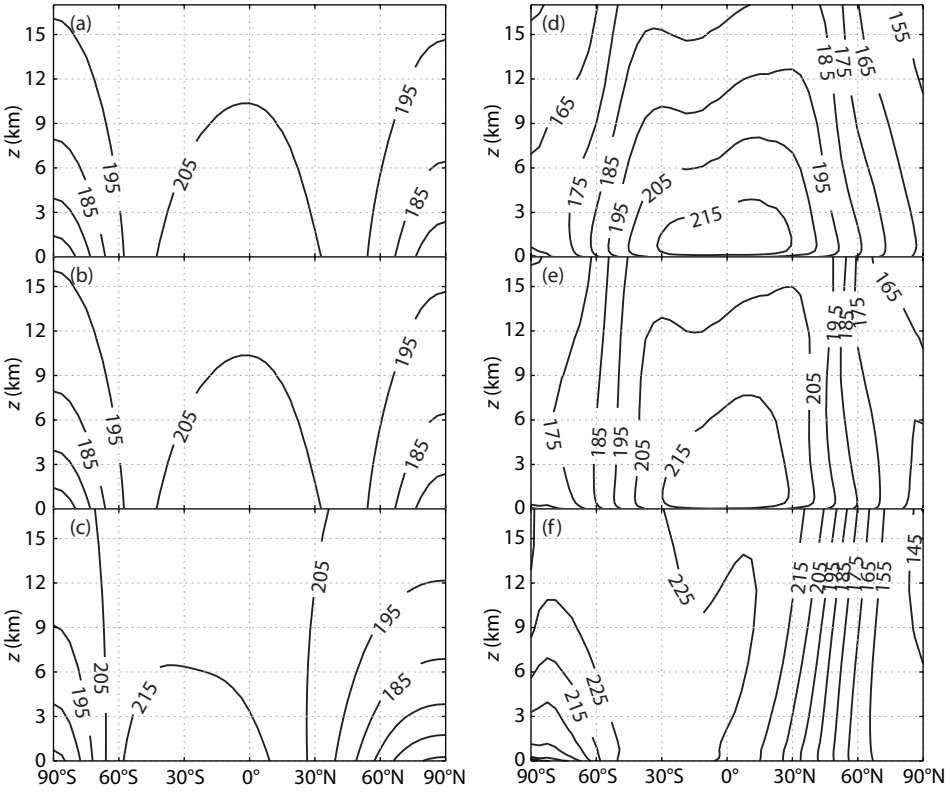

Figure 5. Atmospheric temperature distribution in the cold (a, d), warm (b, e), and storm (c, f) scenarios. Panels (a–c) illustrate the results for the two-dimensional EBM, whereas panels (e–f) for the MCD.

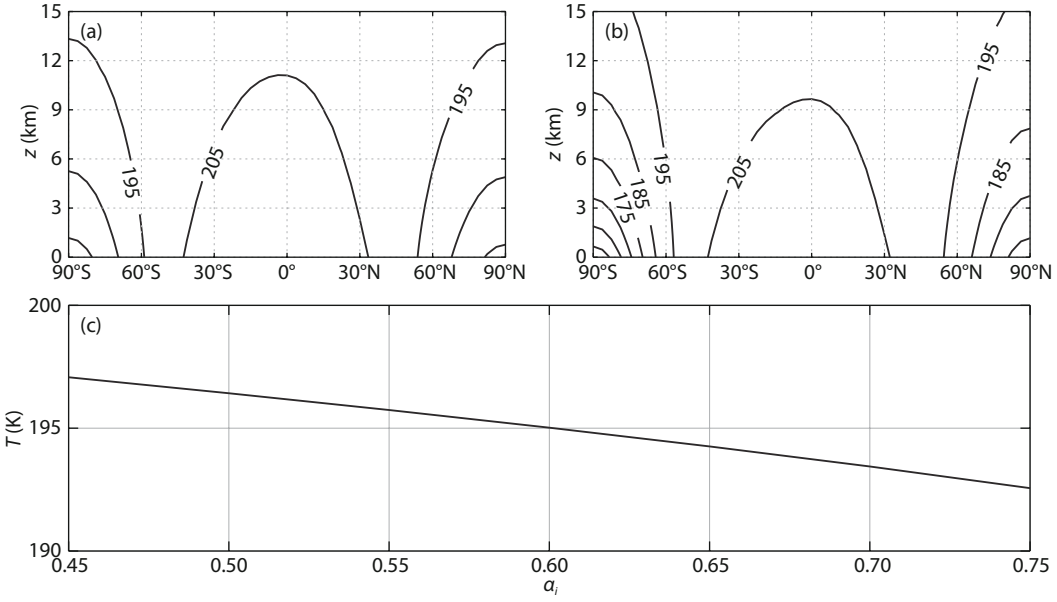

Figure 6. Atmospheric temperature distribution for the albedo values of polar ice of 0.45 (a) and 0.75 (b), respectively; and variation of the mean surface atmospheric temperature with the polar ice albedo (c).

4. Summary and Discussion

We built a latitudinal–vertical EBM for the Martian climate in this study. The model considers the energy balance among the incoming shortwave solar radiation, the outgoing longwave radiation, and the meridional, vertical energy transport. By applying a simplification scheme to deal with the longwave radiation spectrum, we analytically expressed the temperature, a climate indicator, as Legendre polynomials. Given the referenced climatological val-

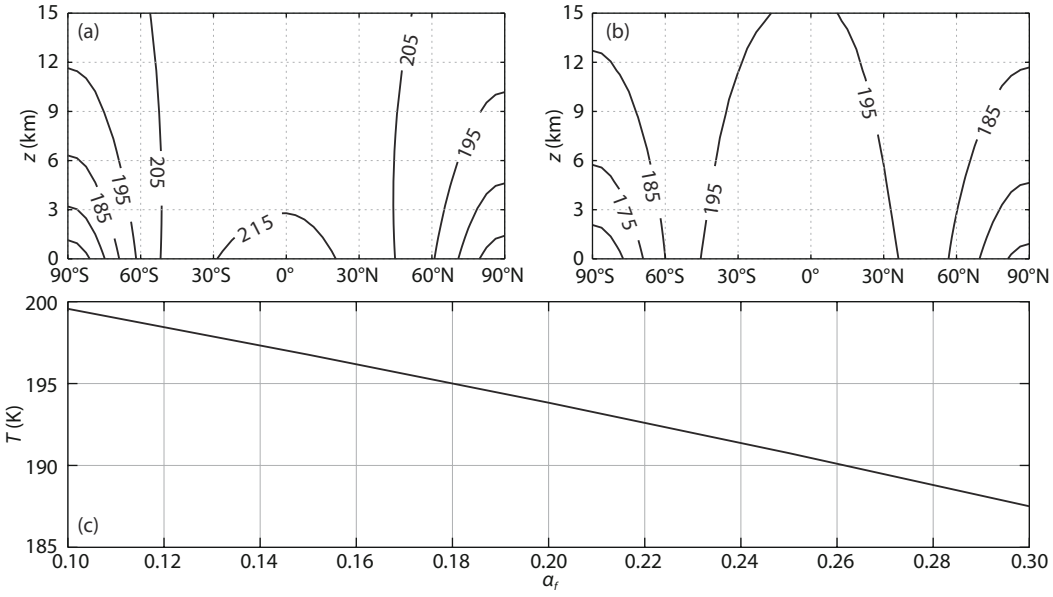

Figure 7. Atmospheric temperature distribution for the albedo values of the non-ice region of 0.1 (a) and 0.3 (b), respectively; and variation of the mean surface atmospheric temperature with the non-ice albedo (c).

ues of all the parameters used, the model can predict a reasonable climate on Mars. Compared with the results of numerical models, such as the MCD, it captures the main features of the mean temperature distribution but has certain distortions, such as the vertical temperature distribution. Generally speaking, it has sufficient reliability to simulate the mean surface atmospheric temperature distribution on Mars. Of course, there are some limitations of and caveats with the model. For example, the dynamic processes in the tropics are not so diffusive; the vertical and horizontal eddy diffusivities were chosen semi-empirically to fit the model simulation with observations; the atmospheric temperature is a steady response to the solar radiation but with no time evolution. We further conducted several experiments to test the ability of the model to simulate the impact of several important parameters, such as the solar radiation distribution, dust concentration, and surface albedo. The basically symmetric solar radiation, such as in months 1 and 7, can force a nearly symmetric temperature distribution, whereas a basically asymmetric solar radiation, such as in months 4 and 10, can obviously lead to an asymmetric temperature distribution. The mean surface temperature declines to minimum values near month 1, when Mars receives the least solar radiation, and it climbs to the maximum value near month 10, when Mars receives the most solar radiation.

Dust can absorb both the solar and longwave radiation to warm Mars. In the cold scenario, the atmospheric temperature varies little compared with its climatological state. In the warm scenario, the atmospheric temperature also shows an insignificant change. We noticed that in both cases, the dust mixing ratio is relatively small. Its absorption for the longwave radiation is relatively small compared to the strong absorption of CO_2, the major component of the Martian atmosphere. However, in the storm scenario, in which the dust mixing ratio has a very high value, dust can warm the atmosphere significantly. The two-dimensional EBM can predict a relatively reasonable surface atmospheric temperature but fails on the vertical distribution. This may be because the vertical distribution of dust is specified in the theoretical model.

The surface albedo plays a negative role in determining the temperature because it can reflect solar radiation. Although polar ice can reflect more solar radiation, the amount of solar radiation itself is smaller in the polar regions and the area of polar ice is also smaller. Therefore, the total amount of reflected solar radiation is relatively smaller than in the non-ice region. An increase of 0.3 in the albedo value of polar ice causes a decrease of 4 K in the mean surface atmospheric temperature, whereas an increase of 0.2 in the albedo value of the non-ice region can lead to a decrease of 13 K in the mean surface air temperature.

These experiments imply that the model can deal with problems associated with solar radiation, dust concentration, and the surface albedo. For example, it can be applied to investigate the evolution of the paleoclimate in different cases of solar radiation. By specifying a temperature corresponding to an ice line, it can further be applied to study the evolution of the polar ice and the equilibrium states of the climate. In addition, by introducing the large-scale atmospheric motion equation, the climatological atmospheric motion can be derived from the basic temperature distribution. This will further extend the application of the model. Finally, the model can be improved by introducing latitudinal variation and by providing a more accurate dust spectrum and surface albedo distribution. This, in turn, depends on continuous observation and investigation on Mars, given that most of the needed observations have actually been accumulated only in the past two decades.

Acknowledgments

The authors sincerely thank Ehouarn Millour for providing the MCD. This study was jointly funded by the National Natural Science Foundation of China (Grant 41505042), the National Program on Global Change and Air–Sea Interaction (Grant GASI-

IPOVAI-03), the National Basis Research Program of China (Grants 2015CB953601, 2014CB953903), and the Fundamental Research Funds for the Central Universities.

References

Appelbaum, J., Landis, G. A., and Sherman, I. (1993). Solar radiation on Mars—Update 1991. *Solar Energy*, *50*(1), 35–51. https://doi.org/10.1016/0038-092X(93)90006-A

Barlow, N. (2014). *Mars: An Introduction to Its Interior, Surface and Atmosphere*. Cambridge, UK: Cambridge University Press.

Barnes, J. R., Haberle, R. M., Pollack, J. B., Lee, H., and Schaeffer, J. (1996). Mars atmospheric dynamics as simulated by the NASA Ames general circulation model: 3. Winter quasi-stationary eddies. *J. Geophys. Res.*: *Planets*, *101*(E5), 12753–12776. https://doi.org/10.1029/96JE00179

Budyko, M. I. (1969). The effect of solar radiation variations on the climate of the earth. *Tellus*, *21*(5), 611–619. https://doi.org/10.3402/tellusa.v21i5.10109

Clifford, S. M., Crisp, D., Fisher, D. A., Herkenhoff, K. E., Smrekar, S. E., Thomas, P. C., Wynn-Williams, D. D., Zurek, R. W., Barnes, J. R., … Jay Zwally, H. (2000). The state and future of Mars polar science and exploration. *Icarus*, *144*(2), 210–242. https://doi.org/10.1006/icar.1999.6290

Conrath, B. J. (1975). Thermal structure of the Martian atmosphere during the dissipation of the dust storm of 1971. *Icarus*, *24*(1), 36–46. https://doi.org/10.1016/0019-1035(75)90156-6

Forget, F., Hourdin, F., Fournier, R., Hourdin, C., Talagrand, O., Collins, M., Lewis, S. R., Read, P. L., and Huot, J. P. (1999). Improved general circulation models of the Martian atmosphere from the surface to above 80 km. *J. Geophys. Res.*: *Planets*, *104*(E10), 24155–24175. https://doi.org/10.1029/1999JE001025

Haberle, R. M., Pollack, J. B., Barnes, J. R., Zurek, R. W., Leovy, C. B., Murphy, J. R., Lee, H., and Schaeffer, J. (1993). Mars atmospheric dynamics as simulated by the NASA Ames General Circulation Model: 1. The zonal-mean circulation. *J. Geophys. Res.*: *Planets*, *98*(E2), 3093–3123. https://doi.org/10.1029/92JE02946

Haberle, R. M., Tyler, D., McKay, C. P., and Davis, W. L. (1994). A model for the evolution of CO_2 on Mars. *Icarus*, *109*(1), 102–120. https://doi.org/10.1006/icar.1994.1079

Haberle, R. M., Clancy, R. T., Forget, F., Smith, M. D., and Zurek, R. W. (2017). *The Atmosphere and Climate of Mars*. Cambridge, UK: Cambridge University Press. https://doi.org/10.1017/9781139060172

Heavens, N. G., Richardson, M. I., Kleinböhl, A., Kass, D. M., McCleese, D. J., Abdou, W., Benson, J. L., Schofield, J. T., Shirley, J. H., and Wolkenberg, P. M. (2011). The vertical distribution of dust in the Martian atmosphere during northern spring and summer: Observations by the Mars Climate Sounder and analysis of zonal average vertical dust profiles. *J. Geophys. Res.*: *Planets*, *116*(E4), E04003. https://doi.org/10.1029/2010JE003691

Heavens, N. G., Kass, D. M., Kleinböhl, A., and Schofield, J. T. (2020). A multiannual record of gravity wave activity in Mars's lower atmosphere from on-planet observations by the Mars Climate Sounder. *Icarus*, *341*, 113630. https://doi.org/10.1016/j.icarus.2020.113630

Hoffert, M. I., Callegari, A. J., Hsieh, C. T., and Ziegler, W. (1981). Liquid water on Mars: An energy balance climate model for CO_2/H_2O atmospheres. *Icarus*, *47*(1), 112–129. https://doi.org/10.1016/0019-1035(81)90096-8

Hollingsworth, J. L., Haberle, R. M., Barnes, J. R., Bridger, A. F. C., Pollack, J. B., Lee, H., and Schaeffer, J. (1996). Orographic control of storm zones on Mars. *Nature*, *380*, 413–416. https://doi.org/10.1038/380413a0

Holmes, J. A., Lewis, S. R., and Patel, M. R. (2020). OpenMARS: A global record of Martian weather from 1999 to 2015. *Planet. Space Sci.*, *188*, 104962. https://doi.org/10.1016/j.pss.2020.104962

James, P. B., and North, G. R. (1982). The seasonal CO_2 cycle on Mars: An application of an energy balance climate model. *J. Geophys. Res.*: *Solid Earth*, *87*(B12), 10271–10283. https://doi.org/10.1029/JB087iB12p10271

Kuo, H. L. (1973). On a simplified radiative-conductive heat transfer equation. *Pure Appl. Geophys.*, *109*(1), 1870–1876. https://doi.org/10.1007/BF00876111

Leovy, C., and Mintz, Y. (1969). Numerical simulation of the atmospheric circulation and climate of Mars. *J. Atmos. Sci.*, *26*(6), 1167–1190. https://doi.org/10.1175/1520-0469(1969)026<1167:NSOTAC>2.0.CO;2

Lewis, S. R., Collins, M., Read, P. L., Forget, F., Hourdin, F., Fournier, R., Hourdin, C., Talagrand, O., and Huot, J. P. (1999). A climate database for Mars. *J. Geophys. Res.*: *Planets*, *104*(E10), 24177–24194. https://doi.org/10.1029/1999JE001024

Li, Y. K., and Chao, J. P. (2014). Two-dimensional energy balance model and its application to some climatic issues. *J. Meteor. Res.*, *28*(5), 747–761. https://doi.org/10.1007/s13351-014-4027-1

Liu, K., Hao, X. J., Li, Y. R., Zhang, T. L., Pan, Z. H., Chen, M. M., Hu, X. W., Li, X., Shen, C. L., and Wang, Y. M. (2020). Mars Orbiter magnetometer of China's First Mars Mission Tianwen-1. *Earth Planet. Phys.*, *4*(4), 384–389. https://doi.org/10.26464/epp2020058

Lü, Y. H., and Chao, J. P. (1981). A climatic theory of temperature distribution of certain planetary atmosphere. *Chin. J. Atmos. Sci.* (*in Chinese*), *5*(2), 145–156. https://doi.org/10.3878/j.issn.1006-9895.1981.02.04

Millour, E., Forget, F., and Lewis, S. R. (2008). Mars Climate Database V4.3 Detailed Design Document.

Montabone, L., Forget, F., Millour, E., Wilson, R. J., Lewis, S. R., Cantor, B., Kass, D., Kleinböhl, A., Lemmon, M. T., … Wolff, M. J. (2015). Eight-year climatology of dust optical depth on Mars. *Icarus*, *251*, 65–95. https://doi.org/10.1016/j.icarus.2014.12.034

Murphy, J. R., Pollack, J. B., Haberle, R. M., Leovy, C. B., Toon, O. B., and Schaeffer, J. (1995). Three-dimensional numerical simulation of Martian global dust storms. *J. Geophys. Res.*: *Planets*, *100*(E12), 26357–26376. https://doi.org/10.1029/95JE02984

Nakamura, T., and Tajika, E. (2001). Stability and evolution of the climate system of Mars. *Earth, Planets, Space*, *53*(8), 851–859. https://doi.org/10.1186/BF03351682

Nakamura, T., and Tajika, E. (2002). Stability of the Martian climate system under the seasonal change condition of solar radiation. *J. Geophys. Res.*: *Planets*, *107*(E11), 5094. https://doi.org/10.1029/2001JE001561

North, G. R. (1975). Analytical solution to a simple climate model with diffusive heat transport. *J. Atmos. Sci.*, *32*(7), 1301–1307. https://doi.org/10.1175/1520-0469(1975)032<1301:ASTASC>2.0.CO;2

Peng, Y. Q., Zhang, L. B., Cai, Z. G., Wang, Z. G., Jiao, H. L., Wang, D. L., Yang, X. T., Wang, L. G., Tan, X., Wang, F., Fang, J., Sun, Z. L., Feng, H. L., Huang, X. R., Zhu, Y., Chen, M., Li, L. H., and Li, Y. H. (2020). Overview of the Mars climate station for Tianwen-1 mission. *Earth Planet. Phys.*, *4*(4), 371–383. https://doi.org/10.26464/epp2020057

Pierrehumbert, R. T. (2010). *Principles of Planetary Climate*. Cambridge, UK: Cambridge University Press. https://doi.org/10.1017/CBO9780511780783

Piqueux, S., Byrne, S., Kieffer, H. H., Titus, T. N., and Hansen, C. J. (2015). Enumeration of Mars years and seasons since the beginning of telescopic exploration. *Icarus*, *251*, 332–338. https://doi.org/10.1016/j.icarus.2014.12.014

Pollack, J. B., Leovy, C. B., Greiman, P. W., and Mintz, Y. (1981). A Martian general circulation experiment with large topography. *J. Atmos. Sci.*, *38*(1), 3–29. https://doi.org/10.1175/1520-0469(1981)038<0003:AMGCEW>2.0.CO;2

Pollack, J. B., Kasting, J. F., Richardson, S. M., and Poliakoff, K. (1987). The case for a wet, warm climate on early Mars. *Icarus*, *71*(2), 203–224. https://doi.org/10.1016/0019-1035(87)90147-3

Pollack, J. B., Haberle, R. M., Schaeffer, J., and Lee, H. (1990). Simulations of the general circulation of the Martian atmosphere: 1. Polar processes. *J. Geophys. Res.*: *Solid Earth*, *95*(B2), 1447–1473. https://doi.org/10.1029/JB095iB02p01447

Read, P. L., Collins, M., Forget, F., Fournier, R., Hourdin, F., Lewis, S. R., Talagrand, O., Taylor, F. W., and Thomas, N. P. J. (1997). A GCM climate database for Mars: For mission planning and for scientific studies. *Adv. Space Res.*, *19*(8), 1213–1222. https://doi.org/10.1016/S0273-1177(97)00272-X

Savijärvi, H. (2014). A toy climate model for Mars. *Icarus*, *242*, 105–111. https://doi.org/10.1016/j.icarus.2014.07.029

Sellers, W. D. (1969). A global climatic model based on the energy balance of the Earth–atmosphere system. *J. Appl. Meteor.*, *8*(3), 392–400. https://doi.org/10.1175/1520-0450(1969)008<0392:AGCMBO>2.0.CO;2

Smith, A. J. R. W., Mandell, A. M., Villanueva, G. L., and Dane Moore, M. (2020).

Utilizing a database of simulated geometric albedo spectra for photometric characterization of rocky exoplanet atmospheres. *Astron. J.*, *160*(5), 204. https://doi.org/10.3847/1538-3881/abb4eb

Smith, M. D. (2004). Interannual variability in TES atmospheric observations of Mars during 1999–2003. *Icarus*, *167*(1), 148–165. https://doi.org/10.1016/j.icarus.2003.09.010

Taubenberger, C. J. (2020). *Energy Balance Models with Realistic Albedo, Monthly Insolation, Milankovitch Cycles, and Simplified Earth-Like Planetary Modeling*. Fairfax, Virginia: George Mason University.

Titus, T. N., and Cushing, G. E. (2014). Monitoring the Mars polar caps during Mars years 24–28. *Presented at 45th Lunar and Planetary Science Conference*. The Woodlands, Texas.

Wang, C., Forget, F., Bertrand, T., Spiga, A., Millour, E., and Navarro, T. (2018). Parameterization of rocket dust storms on mars in the LMD Martian GCM: Modeling details and validation. *J. Geophys. Res.: Planets*, *123*(4), 982–1000. https://doi.org/10.1002/2017JE005255

Wu, Z. P., Richardson, M. I., Zhang, X., Cui, J., Heavens, N. G., Lee, C., Li, T., Lian, Y., Newman, C. E., … Witek, M. (2021). Large eddy simulations of the dusty Martian convective boundary layer with MarsWRF. *J. Geophys. Res.: Planets*, *126*(9), e2020JE006752. https://doi.org/10.1029/2020JE006752